Abstracta

Ano XXIII - N. 04

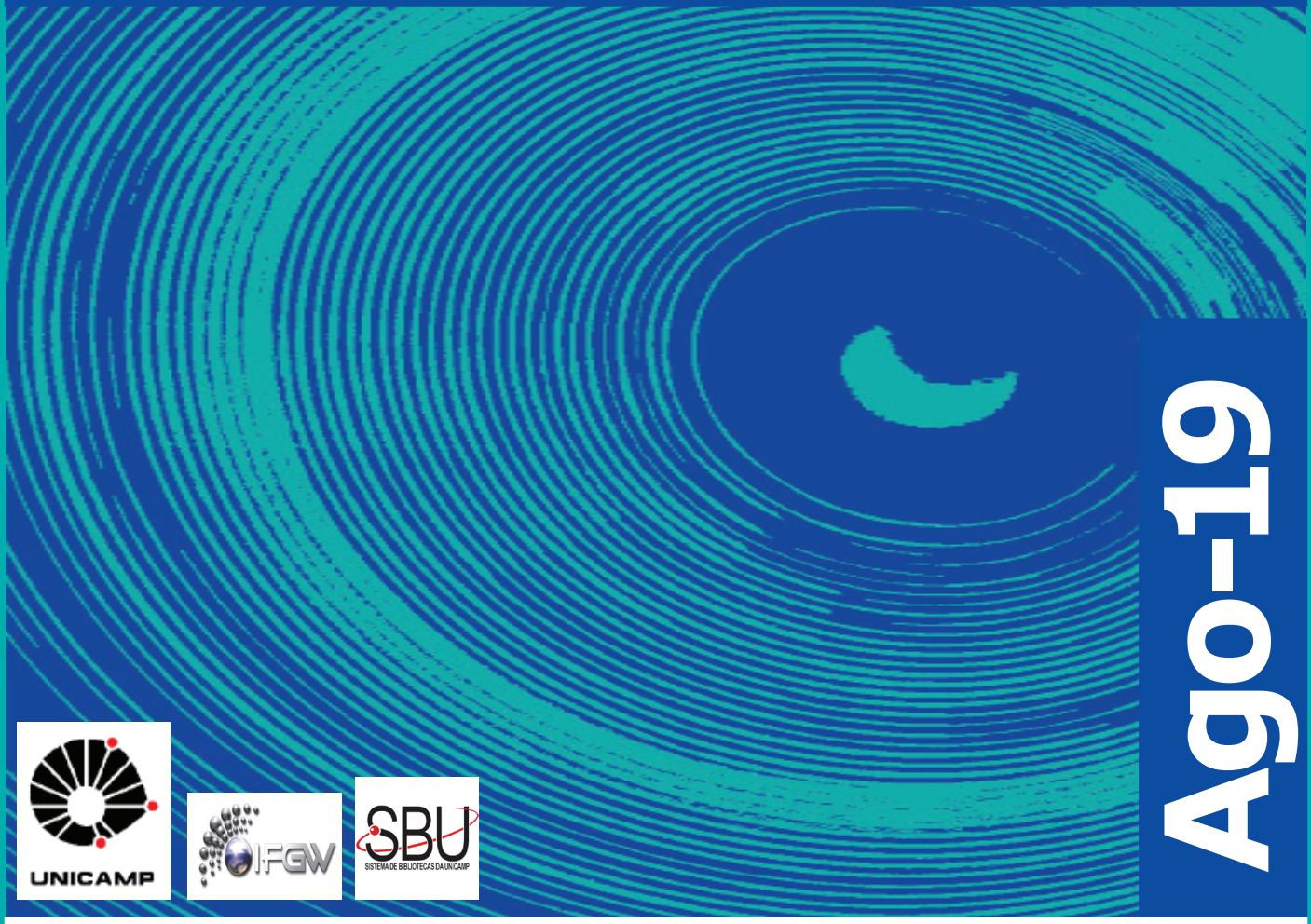

Ago-19

UNICAMP

IFGW

SBU
SISTEMA DE BIBLIOTECAS DA UNICAMP

Artigos publicados - P232-2019 à P295-2019

Eventos publicados - P296-2019 à P297-2019

Defesas de Teses do IFGW - T007-2019

Defesas de Dissertações do IFGW - D015-2019

Artigos publicados

[P232-2019] "A Hi-Bi Ultra-Sensitive Surface Plasmon Resonance Fiber Sensor"

Islam, M. S.; **Cordeiro, C. M. B.***; Sultana, J.; Aoni, R. A.; Feng, S.; Ahmed, R.; Dorraki, M.; Dinovitser, A.; Ng, B. W.-H.; Abbott, D.

In this paper, a simple, miniature, and highly sensitive photonic crystal fiber (PCF)-based surface plasmon resonance (SPR) sensor is proposed. The target analyte and the plasmonic material are at the outer surface of the fiber making practical applications feasible. A 30-nm gold (Au) layer supports surface plasmons. A thin titanium dioxide (TiO2) layer is used to assist adhesion of Au on the glass fiber. The fiber cross section is formed purely by circular-shaped holes simplifying the preform manufacturing process. A high-birefringence (hi-bi) fiber is obtained by means of an array of air holes at the center of the fiber. A finite element method (FEM) is employed to analyze the surface plasmon properties of the proposed PCF-SPR sensor. By optimizing the geometric parameters, a maximum wavelength sensitivity (WS) of 25 000 nm/RIU and an amplitude sensitivity (AS) of 1411 RIU-1 for a dielectric refractive index (RI) range of 1.33-1.38 are obtained. Moreover, an estimated maximum resolution of 4 x 10(-6) and a figure of merit (FOM) of 502 are obtained that ensures high detection accuracy of small refractive index (RI) changes. Owing to its sensitivity and simple architecture, the proposed sensor has potential application in a range of sensing application, including biosensing.

IEEE ACCESS 7, 79085-79094, 2019. DOI: 10.1109/ACCESS.2019.2922663

[P233-2019] "Absence of spin-ice state in the disordered fluorite Dy2Zr2O7"

Ramon, J. G. A.; Wang, C. W.; **Ishida, L.***; Bernardo, P. L.; Leite, M. M.; Vichi, F. M.; Gardner, J. S.; Freitas, R. S.

Neutron scattering, ac magnetic susceptibility, and specific-heat studies have been carried out on polycrystalline Dy2Zr2O7. Unlike the pyrochlore spin ice Dy2Ti2O7, Dy2Zr2O7 crystallizes into the fluorite structure and the magnetic Dy3+ moments randomly reside on the corner-sharing tetrahedral sublattice with nonmagnetic Zr ions. Antiferromagnetic spin correlations develop below 10 K but remain dynamic down to 40 mK, with a significant amount of magnetic susceptibility. These correlations extend over the length of two tetrahedra edges and grow to six nearest neighbors with the application of a 20-kOe magnetic field. Magnetic heat capacity revealed a correlation peak at 2 K, but no Pauling's residual entropy was observed. We propose that the disorder precludes the development of spin-ice correlations seen in the chemically ordered Dy2Ti2O7 compound, with fluctuating spins in a disordered, liquidlike state (albeit slow) which do not freeze into a canonical spin-glass state that one might intuitively expect.

PHYSICAL REVIEW B 99[21], 214442, 2019. DOI: 10.1103/PhysRevB.99.214442

[P234-2019] "An embedding technique to determine tau tau backgrounds in proton-proton collision data"

Sirunyan, A. M.; Tumasyan, A.; Adam, W.; **Chinellato, J. A.*; Tonelli Manganote, E. J.***; et. al.; CMS Collaboration

An embedding technique is presented to estimate standard model tau tau backgrounds from data with minimal simulation input. In the data, the muons are removed from reconstructed mu mu events and replaced with simulated tau leptons with the same kinematic properties. In this way, a set of hybrid events is obtained that does not rely on simulation except for the decay of the tau leptons. The challenges in describing the underlying event or the production of associated jets in the simulation are avoided. The technique described in this paper was developed for CMS. Its validation and the inherent uncertainties are also discussed. The demonstration of the performance of the technique is based on a sample of proton-proton collisions collected by CMS in 2017 at root s = 13 TeV corresponding to an integrated luminosity of 41.5 fb(-1).

JOURNAL OF INSTRUMENTATION 14, P06032, 2019. DOI: 10.1088/1748-0221/14/06/P06032

[P235-2019] "Analysis of the apparent nuclear modification in peripheral Pb-Pb collisions at 5.02 TeV"

Acharya, S.; Acosta, F. T.; Adamova, D.; **Albuquerque, D. S. D.*; Chinellato, D. D.*; De Souza, R. D.*; Takahashi, J.***; et. al.; ALICE Collaboration

Charged-particle spectra at midrapidity are measured in Pb-Pb collisions at the centre-of-mass energy per nucleon-nucleon pair root s(NN) = 5.02 TeV and presented in centrality classes ranging from most central (0-5%) to most peripheral (95-100%) collisions. Possible medium effects are quantified using the nuclear modification factor (R-AA) by comparing the measured spectra with those from proton-proton collisions, scaled by the number of independent nucleon-nucleon collisions obtained from a Glauber model. At large transverse momenta (8 < p(T) < 20 GeV/c), the average R-AA is found to increase from about 0.15 in 0-5% central to a maximum value of about 0.8 in 75-85% peripheral collisions, beyond which it falls off strongly to below 0.2 for the most peripheral collisions. Furthermore, R-AA initially exhibits a positive slope as a function of p(T) in the 8-20 GeV/c interval, while for collisions beyond the 80% class the slope is negative. To reduce uncertainties related to event selection and normalization, we also provide the ratio of R-AA in adjacent centrality intervals. Our results in peripheral collisions are consistent with a PYTHIA-based model without nuclear modification, demonstrating that biases caused by the event selection and collision geometry can lead to the apparent suppression in peripheral collisions. This explains the unintuitive observation that R-AA is below unity in peripheral Pb-Pb, but equal to unity in minimum-bias p-Pb collisions despite similar charged-particle multiplicities.

PHYSICS LETTERS B 793, 420-432, 2019. DOI: 10.1016/j.physletb.2019.04.047

[P236-2019] "Boundary conditions and renormalized stress--energy tensor on a Poincare patch of AdS(2)"

Pitelli, J. P. M.; **Barroso, V. S.***; Mosna, R. A.

Quantum field theory on anti-de Sitter spacetime requires the introduction of boundary conditions at its conformal boundary, due essentially to the absence of global hyperbolicity. Here we calculate the renormalized stress-energy tensor T-mu nu for a scalar field phi on the Poincare patch of AdS(2) and study how it depends on those boundary conditions. We show that, except for the Dirichlet and Neumann cases, the boundary conditions break the maximal AdS invariance. As a result, <phi(2)> acquires a space dependence and < T-mu nu > is no longer proportional to the metric.When the physical quantities are expanded in a parameter beta which characterizes the boundary conditions (with beta = 0 corresponding to Dirichlet and beta = infinity corresponding to Neumann), the singularity of the Green's function is entirely subtracted at zeroth order in beta. As a result, the contribution of nontrivial boundary conditions to the stress-energy tensor is free of singular terms.

PHYSICAL REVIEW D 99[12], 125008, 2019. DOI: 10.1103/PhysRevD.99.125008

[P237-2019] "Broadband enhancement of thermal radiation"

Bhatt, G. R.; Dutt, A.; Miller, S. A.; St-Gelais, R.; **Barbosa, F. A. S.***; Nussenzveig, P. A.; Lipson, M.

Broadband thermal radiation sources are critical for various applications including spectroscopy and electricity generation. However, due to the difficulty in simultaneously achieving high absorptivity and low thermal mass these sources are inefficient. We show a platform that enables one to obtain enhanced emission by coupling a thermal emitter to an optical cavity. We experimentally demonstrate broadband enhancement of thermal emission between lambda similar to 2 - 4.2 mu m using an inherently poor thermal emitter consisting of tens of nanometers thick SiC film with 10% emissivity (epsilon(S)(iC) similar to 0.1). We measure over twofold enhancement of total emission power over the entire spectral band and threefold enhancement of thermal emission over 3 to 3.4 mu m. Our platform has the potential to enable development of ideal blackbody sources operating at substantially lower heating powers.

OPTICS EXPRESS 27[12], A818-A828, 2019. DOI: 10.1364/OE.27.00A818

[P238-2019] "Calibration of the photon spectrometer PHOS of the ALICE experiment"

Acharya, S.; Acosta, F. T.; Adamova, D.; **Albuquerque, D. S. D.*; Chinellato, D. D.*; De Souza, R. D.*; Takahashi, J.***; et. al.; ALICE Collaboration

The procedure for the energy calibration of the high granularity electromagnetic calorimeter PHOS of the ALICE experiment is presented. The methods used to perform the relative gain calibration, to evaluate the geometrical alignment and the corresponding correction of the absolute energy scale, to obtain the nonlinearity correction coefficients and finally, to calculate the time-dependent calibration corrections, are discussed and illustrated by the PHOS performance in proton-proton (pp) collisions at root s = 13 TeV. After applying all corrections, the achieved mass resolutions for pi(0) and eta mesons for p(T) > 1.7 GeV/c are sigma(pi 0)(m) = 4.56 +/- 0.03 MeV/c(2) and sigma(eta)(m) = 15.3 +/- 1.0 MeV/c(2), respectively.

JOURNAL OF INSTRUMENTATION 14, P05025, 2019. DOI: 10.1088/1748-0221/14/05/P05025

[P239-2019] "Castration-induced prostate epithelial cell apoptosis results from targeted oxidative stress attack of M1(142)-macrophages"

Barbosa, G. O.; Silva, J. A. F.; Siqueira-Berti, A.; Nishan, U.; Rosa-Ribeiro, R.; Oliveira, S. B. P.; Baratti, M. O.; Ferrucci, D.; Santana, J. C. O.; Damas-Souza, D. M.; Bruni-Cardoso, A.; Augusto, T. M.; Correa-da-Silva, F.; Moraes-Vieira, P. M.; Stach-Machado, D. R.; Felisbino, S. L.; Menezes, G. B.; **Cesar, C. L.***; Carvalho, H. F.

Prostate development and function are regulated by androgens. Epithelial cell apoptosis in response to androgen deprivation is caspase-9-dependent and peaks at Day 3 after castration. However, isolated epithelial cells survive in the absence of androgens. Znf142 showed an on-off expression pattern in intraepithelial CD68-positive macrophages, with the on-phase at Day 3 after castration. Rats treated with gadolinium chloride to deplete macrophages showed a significant drop in apoptosis, suggesting a causal relationship between macrophages and epithelial cell apoptosis. Intraepithelial M1-polarization was also limited to Day 3, and the inducible nitric oxide synthase (iNOS) knockout mice showed significantly less apoptosis than wild-type controls. The epithelial cells showed focal DNA double-strand breaks (DSB), 8-oxoguanine, and protein tyrosine-nitrosylation, fingerprints of exposure to peroxinitrite. Cultured epithelial cells induced M1-polarization and showed focal DSB and underwent apoptosis. The same phenomena were reproduced in LNCaP cells cocultured with Raw 264.7 macrophages. In conclusion, the M1 (142)-macrophage (named after Znf142) attack causes activation of the intrinsic apoptosis pathway in epithelial cells after castration.

JOURNAL OF CELLULAR PHYSIOLOGY 234, [10], 19048-19058, 2019. DOI: 10.1002/jcp.28544

[P240-2019] "Changes of functional response in sensorimotor cortex of preterm and full-term infants during the first year: An fNIRS study"

de Oliveira, S. R.; Machado, A. C. C. P.; de Paula, J. J.; **Novi, S. L.*; Mesquita, R. C.***; de Miranda, D. M.; Bouzada, M. C. F.

Background: Motor impairments are frequently associated with preterm birth and interfere in acquisition of essential skills to global development. Using Near Infrared Spectroscopy (NIRS), the study of neural correlates of motor development in early stages of life are feasible in an ecological assessment. Aims: To evaluate changes in cortical activity in response to a sensorimotor stimulation in preterm and full-term infants at 6 and 12 months of age. Study design: A longitudinal study was conducted with 22 infants (12 preterm and 10 full-term). Hemodynamic activity during sensorimotor task (8 blocks of 8 s of vibration applied to infant's right hand) was measured by Functional Near Infrared Spectroscopy (fNIRS). The optical probe consisted of 84 channels positioned according to the international 10-20 system coordinates, covering the frontal (38 channels), parietal (16 channels), temporal (22 channels) and occipital (8 channels) lobes of both hemispheres. Results: Preterm and full-term infants exhibited differences of location of the activation as well on the hemodynamic response in both the evaluated age groups. Conclusions: Group differences in activation of sensorimotor cortex observed in this study demonstrate the potential of fNIRS application for preterm evaluation of motor development in children. Overall, the present work contributes to our understanding of cortical activation of cerebral motor skills spanning early ages in preterm-born children.

EARLY HUMAN DEVELOPMENT 133, 23-28, 2019. DOI: 10.1016/j.earlhumdev.2019.04.007

[P241-2019] "Combinations of single-top-quark production cross-section measurements and vertical bar f(LV)V(tb) vertical bar determinations at root s=7 and 8 TeV with the ATLAS and CMS experiments"

Aaboud, M.; Aad, G.; Abbott, B.; **Chinellato, J. A.*; Tonelli Manganote, E. J.***; et. al.; ATLAS Collaboration; ATLAS Collaboration; CMS Collaboration

This paper presents the combinations of single-top-quark production cross-section measurements by the ATLAS and CMS Collaborations, using data from LHC proton-proton collisions at = 7 and 8 TeV corresponding to integrated luminosities of 1.17 to 5.1 fb(-1) at = 7 TeV and 12.2 to 20.3 fb(-1) at = 8 TeV. These combinations are performed per centre-of-mass energy and for each production mode: t-channel, tW, and s-channel. The combined t-channel cross-sections are 67.5 +/- 5.7 pb and 87.7 +/- 5.8 pb at = 7 and 8 TeV respectively. The combined tW cross-sections are 16.3 +/- 4.1 pb and 23.1 +/- 3.6 pb at = 7 and 8 TeV respectively. For the s-channel cross-section, the combination yields 4.9 +/- 1.4 pb at = 8 TeV. The square of the magnitude of the CKM matrix element V-tb multiplied by a form factor f(LV) is determined for each production mode and centre-of-mass energy, using the ratio of the measured cross-section to its theoretical prediction.

It is assumed that the top-quark-related CKM matrix elements obey the relation |V-td|, |V-ts| << |V-tb|. All the |f(LV)V(tb)|(2) determinations, extracted from individual ratios at = 7 and 8 TeV, are combined, resulting in |f(LV)V(tb)| = 1.02 +/- 0.04 (meas.) +/- 0.02 (theo.). All combined measurements are consistent with their corresponding Standard Model predictions.

JOURNAL OF HIGH ENERGY PHYSICS 5, 088, 2019. DOI: 10.1007/JHEP05(2019)088

[P242-2019] "Combined measurements of Higgs boson couplings in proton- proton collisions at v s=13TeV"

Sirunyan, A. M.; Tumasyan, A.; Adam, W.; **Chinellato, J. A.*; Tonelli Manganote, E. J.***; et. al.; CMS Collaboration

Combined measurements of the production and decay rates of the Higgs boson, as well as its couplings to vector bosons and fermions, are presented. The analysis uses the LHC proton-proton collision data set recorded with the CMS detector in 2016 at fb-1. The combination is based on analyses targeting the five main Higgs boson production mechanisms (gluon fusion, vector boson fusion, and associated production with a W or Z boson, or a top quark-antiquark pair) and the following decay modes: H, ZZ, WW, , bb, and . Searches for invisible Higgs boson decays are also considered. The best-fit ratio of the signal yield to the standard model expectation is measured to be =1.17 +/- 0.10, assuming a Higgs boson mass of 125.09. Additional results are given for various assumptions on the scaling behavior of the production and decay modes, including generic parametrizations based on ratios of cross sections and branching fractions or couplings. The results are compatible with the standard model predictions in all parametrizations considered. In addition, constraints are placed on various two Higgs doublet models.

EUROPEAN PHYSICAL JOURNAL C 79[5], 421, 2019. DOI: 10.1140/epjc/s10052-019-6909-y

[P243-2019] "Cosmological lensing ratios with DES Y1, SPT, and Planck"

Prat, J.; Baxter, E.; Shin, T.; **Sobreira, F.***; et. al.; DES Collaboration; SPT Collaboration

Correlations between tracers of the matter density field and gravitational lensing are sensitive to the evolution of the matter power spectrum and the expansion rate across cosmic time. Appropriately defined ratios of such correlation functions, on the other hand, depend only on the angular diameter distances to the tracer objects and to the gravitational lensing source planes. Because of their simple cosmological dependence, such ratios can exploit available signal-to-noise ratio down to small angular scales, even where directly modelling the correlation functions is difficult. We present a measurement of lensing ratios using galaxy position and lensing data from the Dark Energy Survey, and CMB lensing data from the South Pole Telescope and Planck, obtaining the highest precision lensing ratio measurements to date. Relative to the concordance Lambda CDM model, we find a best-fitting lensing ratio amplitude of A = 1.1 +/- 0.1. We use the ratio measurements to generate cosmological constraints, focusing on the curvature parameter. We demonstrate that photometrically selected galaxies can be used to measure lensing ratios, and argue that future lensing ratio measurements with data from a combination of LSST and Stage-4 CMB experiments can be used to place interesting cosmological constraints, even after considering the systematic uncertainties associated with photometric redshift and galaxy shear estimation.

MONTHLY NOTICES OF THE ROYAL ASTRONOMICAL SOCIETY 487[1], 1363-1379, 2019. DOI: 10.1093/mnras/stz1309

[P244-2019] "Dark Energy Survey year 1 results: Constraints on extended cosmological models from galaxy clustering and weak lensing"

Abbott, T. M. C.; Abdalla, F. B.; Avila, S.; **Sobreira, F.***; et. al.; DES Collaboration

We present constraints on extensions of the minimal cosmological models dominated by dark matter and dark energy, Lambda CDM and wCDM, by using a combined analysis of galaxy clustering and weak gravitational lensing from the first-year data of the Dark Energy Survey (DES Y1) in combination with external data. We consider four extensions of the minimal dark energy-dominated scenarios: (1) nonzero curvature Omega(k), (2) number of relativistic species N-eff different from the standard value of 3.046, (3) time-varying equation-of-state of dark energy described by the parameters w(0) and w(a) (alternatively quoted by the values at the pivot redshift, w(p), and w(a)), and (4) modified gravity described by the parameters is mu(0) and Sigma(0) that modify the metric potentials. We also consider external information from Planck cosmic microwave background measurements; baryon acoustic oscillation measurements from SDSS, 6dF, and BOSS; redshift-space distortion measurements from BOSS; and type Ia supernova information from the Pantheon compilation of datasets. Constraints on curvature and the number of relativistic species are dominated by the external data; when these are combined with DES Y1, we find Omega(k) = 0.0020(-0.0032)(+0.0037) at the 68% confidence level, and the upper limit N-eff < 3.28(3.55) at 68% (95%) confidence, assuming a hard prior N-eff > 3.0. For the time-varying equation-of-state, we find the pivot value (w(p), w(a)) = (-0.91(-0.23)(+0.19), -0.57(-1.11)(+0.93)) at pivot redshift z(p)= 0.27 from DES alone, and (w(p), w(a)) = (-1.01(-0.04)(+0.04), -0.28(-0.48)(+0.37)) at z(p) = 0.20 from DES Y1 combined with external data; in either case we find no evidence for the temporal variation of the equation of state. For modified gravity, we find the present-day value of the relevant parameters to be Sigma(0) = 0.43(-)(0.29)(+0.28) from DES Y1 alone, and (Sigma(0), mu(0)) = (0.06(-0.07)(+0.08), -0.11(-0.46)(+0.42)) from DES Y1 combined with external data. These modified-gravity constraints are consistent with predictions from general relativity.

PHYSICAL REVIEW D 99[12], 123505, 2019. DOI: 10.1103/PhysRevD.99.123505

[P245-2019] "Efficient Aerobic Oxidation of trans-2-Hexen-1-ol using the Aryl Alcohol Oxidase from Pleurotus eryngii"

de Almeida, T. P.; van Schie, M. M. C. H.; Ma, A.; Tieves, F.; Younes, S. H. H.; Fernandez-Fueyo, E.; Arends, I. W. C. E.; **Riul, A., Jr.***; Hollmann, F.

The selective oxidation of trans-2-hexen-1-ol to the corresponding aldehyde using a recombinant aryl alcohol oxidase from Pleurotus eryngii (PeAAOx) is reported. Especially using the two liquid phase system to overcome solubility and product inhibition issues enabled to achieve more than 2.200.000 catalytic turnovers for the production enzyme as well as molar product concentrations, pointing towards an economic feasible reaction.

ADVANCED SYNTHESIS & CATALYSIS 361[11], (SI), 2668-2672, 2019. DOI: 10.1002/adsc.201801312

[P246-2019] "Elastic and 'transparent bone' as an electrochemical separator"

Owuor, P. S.; Inthong, S.; Sajadi, S. M.; Intawin, P.; Chipara, A. C.; **Woellner, C. F.***; Sayed, F. N.; Tsang, H. H.; Stender, A.; Vajtai, R.; Pengpat, K.; Eitssayeam, S.; **Galvao, D. S.***; Lou, J.; Tiwary, C. S.; Ajayan, P. M.

The organic matrix of a bone mainly composed of a collagen matrix serves as a crucial component for remarkable toughness and strength in bones. The porous collagen matrix can also serve as an efficient template for various applications such as nanoparticle synthesis, catalysis or catalysis supports, electrochemical separator, filtration membrane, and tissue engineering. However, fabricating collagen matrix from bones without degrading its morphological structure still remains a challenge. Here, we present evidence of how ceramic crystals from a bone can be removed to fabricate a complete 'transparent bone' structure with improved porosity and elasticity. We show that demineralization or selective etching using dilute acid (citric) can remove ceramic mineral nanoparticles without degrading the collagen matrix. The transparent bone collagen matrix is investigated as the separator in electrochemical supercapacitor with aqueous electrolyte where it shows better performance compared with conventional separators.

MATERIALS TODAY CHEMISTRY 12, 132-138, 2019. DOI: 10.1016/j.mtchem.2018.12.009

[P247-2019] "Entanglement entropy for the valence bond solid phases of two-dimensional dimerized Heisenberg antiferromagnets"

Leite, L. S. G.*; Doretto, R. L.*

We calculate the bipartite von Neumann and second Renyi entanglement entropies of the ground states of spin-1/2 dimerized Heisenberg antiferromagnets on a square lattice. Two distinct dimerization patterns are considered: columnar and staggered. In both cases, we concentrate on the valence bond solid (VBS) phase and describe such a phase with the bond--operator representation. Within this formalism, the original spin Hamiltonian is mapped into an effective interacting boson model for the triplet excitations. We study the effective Hamiltonian at the harmonic approximation and determine the spectrum of the elementary triplet excitations. We then follow an analytical procedure, which is based on a modified spin-wave theory for finite systems and was originally employed to calculate the entanglement entropies of magnetic ordered phases, and calculate the entanglement entropies of the VBS ground states. In particular, we consider one-dimensional (line) subsystems within the square lattice, a choice that allows us to consider line subsystems with sizes up to L' = 1000. We combine such a procedure with the results of the bond-operator formalism at the harmonic level and show that, for both dimerized Heisenberg models, the entanglement entropies of the corresponding VBS ground states obey an area law as expected for gapped phases. For both columnar-dimer and staggered-dimer models, we also show that the entanglement entropies increase but they seem to not diverge as the dimerization decreases and the system approaches the Neel-VBS quantum phase transition. Finally, the entanglement spectra associated with the VBS ground states are presented.

PHYSICAL REVIEW B 100[4], 045113, 2019. DOI: 10.1103/PhysRevB.100.045113

[P248-2019] "Evaluation of early radiation DNA damage in a fractal cell nucleus model using Geant4-DNA"

Sakata, D.; Lampe, N.; Karamitros, M.; Kyriakou, I.; Belov, O.; **Bernal, M. A.*;** Bolst, D.; Bordage, M. C.; Breton, B., Jeremy M. C.; Francis, Z.; Ivanchenko, V.; Meylan, M. K.; Okada, S.; Petrovic, I.; Ristic-Fira, A.; Santin, G.; Sarramia, D.; Sasaki, T.; Shin, W. G.; Tang, N.; Tran, H. N.; Villagrasa, C.; Emfietzoglou, D.; Nieminen, P.; Guatelli, S.; Incerti, S.

The advancement of multidisciplinary research fields dealing with ionising radiation induced biological damage - radiobiology, radiation physics, radiation protection and, in particular, medical physics - requires a clear mechanistic understanding of how cellular damage is induced by ionising radiation. Monte Carlo (MC) simulations provide a promising approach for the mechanistic simulation of radiation transport and radiation chemistry, towards the in silico simulation of early biological damage. We have recently developed a fully integrated MC simulation that calculates early single strand breaks (SSBs) and double strand breaks (DSBs) in a fractal chromatin based human cell nucleus model. The results of this simulation are almost equivalent to past MC simulations when considering direct/indirect strand break fraction, DSB yields and fragment distribution. The simulation results agree with experimental data on DSB yields within 13.6% on average and fragment distributions agree within an average of 34.8%.

PHYSICA MEDICA-EUROPEAN JOURNAL OF MEDICAL PHYSICS 62, 152-157, 2019. DOI: 10.1016/j.ejmp.2019.04.010

[P249-2019] "Fe3O4@SiO2 Nanoparticles Concurrently Coated with Chitosan and GdOF:Ce3+,Tb3+ Luminophore for Bioimaging: Toxicity Evaluation in the Zebrafish Model"

Khan, L. U.; da Silva, G. H.; de Medeiros, A. M. Z.; Khan, Z. U.; Gidlund, M.; Brito, H. F.; **Moscoso-Londono, O.*; Muraca, D.*; Knobel, M.*;** Perez, C. A.; Martinez, D. S. T.

In this work, design and physiochemical characterization of a biocompatible nanoplatform with integrated photoluminescence and magnetic properties were reported. The potential in vivo toxicity was assessed by exploring the biodistribution of nanoparticles using synchrotron X-ray fluorescence (SXRF) imaging in the zebrafish embryos as a biological model. Their synthesis is accessible through combining magnetic iron oxide nanoparticles with Ce3+, and Tb3+ -doped GdOF luminophore and concurrent capping in situ with chitosan biopolymer. The Fe3O4@SiO2/GdOF:xCe(3+),yTb(3+) nanoparticles manifested near superparamagnetic behavior at 300 K, displaying green emission lines, arising from the characteristic D-5(4) -> F-7(J) transitions (J = 6-0) of Tb3+ ion. The limited permeability of the chorion membrane is a critical factor in toxicity screening, a potential approach to remove the chorion and expose the chorion-off zebrafish embryos to nanoscale materials. Accordingly, multifunctional nanoparticles exhibited no acute toxicity to the with-chorion and chorion-off zebrafish embryos up to 100 mg L-1 exposure concentration, suggesting remarkable in vivo biocompatibility. By assessing the nanobio interaction via deep-tissue SXRF imaging, it was visualized that the distribution of Gd and Fe elements had occurred with a roughly constant relative ratio in the whole body of early-stage embryos. However, the elements mapping data revealed a predominant localization of Gd and Fe in the gastrointestinal tract, manifesting bioaccumulation of magneto-luminescent nanoparticles as an integrated nanoplatform in the respective region. This result demonstrated that the particles uptake by embryos were mostly through oral exposure rather than the dermal pathway, offering a new route to oral administration of nanoparticles for future biological and environmental applications.

ACS APPLIED NANO MATERIALS 2[6], 3414-3425, 2019. DOI: 10.1021/acsanm.9b00339 **(Artigo destaque de capa)**

[P250-2019] "First cosmological results using Type Ia supernovae from the Dark Energy Survey: measurement of the Hubble constant"

Macaulay, E.; Nichol, R. C.; Bacon, D.; **Sobreira, F.*;** et al. DES Collaboration

We present an improved measurement of the Hubble constant (H-0) using the 'inverse distance ladder' method, which adds the information from 207 Type Ia supernovae (SNe Ia)

from the Dark Energy Survey (DES) at redshift 0.018 < z < 0.85 to existing distance measurements of 122 low-redshift (z < 0.07) SNe Ia (Low-z) and measurements of Baryon Acoustic Oscillations (BAOs). Whereas traditional measurements of H-0 with SNe Ia use a distance ladder of parallax and Cepheid variable stars, the inverse distance ladder relies on absolute distance measurements from the BAOs to calibrate the intrinsic magnitude of the SNe Ia. We find H-0 = 67.8 +/- 1.3 km s(-1) Mpc(-1) (statistical and systematic uncertainties, 68 per cent confidence). Our measurement makes minimal assumptions about the underlying cosmological model, and our analysis was blinded to reduce confirmation bias. We examine possible systematic uncertainties and all are below the statistical uncertainties. Our H-0 value is consistent with estimates derived from the Cosmic Microwave Background assuming a Lambda CDM universe.

MONTHLY NOTICES OF THE ROYAL ASTRONOMICAL SOCIETY 486[2], 2184-2196, 2019. DOI: 10.1093/mnras/stz978

[P251-2019] "First cosmology results using Type IA supernovae from the dark energy survey: effects of chromatic corrections to supernova photometry on measurements of cosmological parameters"

Lasker, J.; Kessler, R.; Scolnic, D.; **Sobreira, F.***; et al. DES Collaboration

Calibration uncertainties have been the leading systematic uncertainty in recent analyses using Type Ia supernovae (SNe Ia) to measure cosmological parameters. To improve the calibration, we present the application of spectral energy distribution-dependent 'chromatic corrections' to the SN light-curve photometry from the Dark Energy Survey (DES). These corrections depend on the combined atmospheric and instrumental transmission function for each exposure, and they affect photometry at the 0.01mag (1 per cent) level, comparable to systematic uncertainties in calibration and photometry. Fitting our combined DES and low-z SN Ia sample with baryon acoustic oscillation (BAO) and cosmic microwave background (CMB) priors for the cosmological parameters Omega(m) (the fraction of the critical density of the universe comprised of matter) and w (the dark energy equation of state parameter), we compare those parameters before and after applying the corrections. We find the change in w and Omega(m) due to not including chromatic corrections is -0.002 and 0.000, respectively, for the DES-SN3YR sample with BAO and CMB priors, consistent with a larger DES-SN3YR-like simulation, which has a w-change of 0.0005 with an uncertainty of 0.008 and an Omega(m) change of 0.000 with an uncertainty of 0.002. However, when considering samples on individual CCDs we find large redshift-dependent biases (similar to 0.02 in distance modulus) for SN distances.

MONTHLY NOTICES OF THE ROYAL ASTRONOMICAL SOCIETY 485[4], 5329-5344, 2019. DOI: 10.1093/mnras/stz619

[P252-2019] "Gasoline Quality Sensor Based on Tilted Fiber Bragg Gratings"

Aristilde, S.*; Cordeiro, C. M. B.*; Osorio, J. H.*

We report on the study of an intensity-based optical fiber sensor for gasoline quality monitoring. The sensor setup employs two Bragg gratings with different spectral responses to interrogate the optical response of a tilted Bragg grating. The sensor operation is based on the tilted Bragg grating sensitivity to external refractive index changes, which are translated as power variations by the interrogation scheme. Gasoline-ethanol solutions with concentrations ranging from 0% to 60% ethanol were used to demonstrate the sensor performance. The results allowed to estimate that the sensor is able, within its resolution limit, to detect ethanol concentration variations of 1.5% in gasoline-ethanol solutions and discriminate temperature variations of 0.5 degrees C. The all-optical sensor setup is compact and robust, making it a competitive alternative for the realization of fuel quality analyses in practical applications.

PHOTONICS 6[2], 51, 2019. DOI: 10.3390/photonics6020051

[P253-2019] "Gravitational waves from binary axionic black holes"

Pacheco, J. A. F.; **Carneiro, S.***; Fabris, J. C.

In a recent paper we have shown that a minimally coupled, self-interacting scalar field of mass m can form black holes of mass M=/(4m) (in Planck units). If dark matter is composed by axions, they can form miniclusters that for QCD axions have masses below this value. In this work it is shown that for a scenario in which the axion mass depends on the temperature as mT-6, minicluster masses above 0.32M, corresponding to an axion mass of 3x10-10 eV, exceed M and can collapse into black holes. If a fraction of these black holes is in binary systems, gravitational waves emitted during the inspiral phase could be detected by advanced interferometers like LIGO or VIRGO and by the planned Einstein Telescope. For a detection rate of one event per year, the lower limits on the binary fraction are 10-4 and 10-6 for LIGO and Einstein Telescope respectively.

EUROPEAN PHYSICAL JOURNAL C 79[5], 426, 2019. DOI: 10.1140/epjc/s10052-019-6940-z

[P254-2019] "Hybrid MoS2/h-BN Nanofillers As Synergic Heat Dissipation and Reinforcement Additives in Epoxy Nanocomposites"

Ribeiro, H.; Trigueiro, J. P. C.; Silva, W. M.; **Woellner, C. F.***; Owuor, P. S.; Chipara, A. C.; Lopes, M. C.; Tiwary, C. S.; Pedrotti, J. J.; Salvatierra, R. V.; Tour, J. M.; Chopra, N.; Odeh, I. N.; Silva, G. G.; Ajayan, P. M.

Two-dimensional (2D) nanomaterials as molybdenum disulfide (MoS2), hexagonal boron nitride (h-BN), and their hybrid (MoS2/h-BN) were employed as fillers to improve the physical properties of epoxy composites. Nano composites were produced in different concentrations and studied in their microstructure, mechanical and thermal properties. The hybrid 2D mixture imparted efficient reinforcement to the epoxy leading to increases of up to 95% in tensile strength, 60% in ultimate strain, and 58% in Young's modulus. Moreover, an enhancement of 203% in thermal conductivity was achieved for the hybrid composite as compared to the pure polymer. The incorporation of MoS2/h-BN mixture nanofillers in epoxy resulted in nanocomposites with multifunctional characteristics for applications that require high mechanical and thermal performance.

ACS APPLIED MATERIALS & INTERFACES 11[27], 24485-24492, 2019. DOI: 10.1021/acsami.7b09945

[P255-2019] "Hydrated excess protons and their local hydrogen bond transport network as measured by translational, librational, and vibrational frequencies"

Teschke, O.*; de Castro, J. R.*; Gomes, W. E.; **Soares, D. M.***

A clear molecular description of excess hydrated protons and their local hydrogen bond transport network remains elusive. Here, the hydrogen bond network of excess hydrated protons in water bridges was probed by measuring their Raman spectra and comparing them to the spectra of protons in ice and water.

The proton vibrational spectrum and the hydrogen bond network translational and librational spectra were recorded. The spectra of the water bridge and water exhibit clear differences, indicating the presence of a structure in water bridges when subjected to an electric field of approximate to 10(6) V/m that has not been previously reported. The intermolecular Raman spectrum of the floating water bridge exhibits a hydrogen bond stretching band at 150-250 cm(-1), librational bands within the 300-1000 cm(-1) spectral range, and a large band at 1500-3000 cm(-1), which corresponds to the vibrational signature of excess hydrated protons in the water bridge structure. The excess protons are shown to move predominantly at the air/water interface, and the effect of this distribution is a measurable change in the air/water interfacial tension from approximate to 80 to approximate to 32 N/m. Therefore, hydrated protons must have a unique water arrangement that enables them to propagate without sinking into bulk water. This local polarized hydrogen bond network in the interfacial water region is characterized by a translational spectrum similar to that of ice V.

JOURNAL OF CHEMICAL PHYSICS 150[23], 234501, 2019. DOI: 10.1063/1.5098314

[P256-2019] "Identification of RR Lyrae Stars in Multiband, Sparsely Sampled Data from the Dark Energy Survey Using Template Fitting and Random Forest Classification"

Stringer, K. M.; Long, J. P.; Macri, L. M.; **Sobreira, F.***; et. al.; DES Collaboration

Many studies have shown that RR Lyrae variable stars (RRL) are powerful stellar tracers of Galactic halo structure and satellite galaxies. The Dark Energy Survey (DES), with its deep and wide coverage (g similar to 23.5 mag in a single exposure; over 5000 deg(2)) provides a rich opportunity to search for substructures out to the edge of the Milky Way halo. However, the sparse and unevenly sampled multiband light curves from the DES wide-field survey (a median of four observations in each of grizY over the first three years) pose a challenge for traditional techniques used to detect RRL. We present an empirically motivated and computationally efficient template-fitting method to identify these variable stars using three years of DES data. When tested on DES light curves of previously classified objects in SDSS stripe 82, our algorithm recovers 89% of RRL periods to within 1% of their true value with 85% purity and 76% completeness. Using this method, we identify 5783 RRL candidates, similar to 28% of which are previously undiscovered. This method will be useful for identifying RRL in other sparse multiband data sets.

ASTRONOMICAL JOURNAL 158[1], 16, 2019. DOI: 10.3847/1538-3881/ab1f46

[P257-2019] "Identifying individuals using fNIRS-based cortical connectomes"

Rodrigues, J. de S.; Ribeiro, F. L.; Sato, J. R.; **Mesquita, R. C.***; Biazoli Jr., C. E.

The fMRI-based functional connectome was shown to be sufficiently unique to allow individual identification (fingerprinting). We aimed to test whether a fNIRS-based connectome could also be used to identify individuals. Forty-four participants performed experimental protocols that consisted of two periods of resting-state interleaved by a cognitive task period. Connectome identification was performed for all possible pairwise combinations of the three periods. The influence of hemodynamic global variation was tested using global signal regression and principal component analysis. High identification accuracies well-above chance level (2.3%) were observed overall, being particularly high (93%) to the oxyhemoglobin signal between resting conditions. Our results suggest that fNIRS is a suitable technique to assess connectome fingerprints.

BIOMEDICAL OPTICS EXPRESS 10[6], 2889-2897, 2019. DOI: 10.1364/BOE.10.002889

[P258-2019] "Impact of standard neutrino oscillations and systematics on proton lifetime measurements"

Gratieri, D. R.*; Guzzo, M. M.*; Peres, O. L. G.*

We use atmospheric neutrino phenomenology to obtain the expected background to proton decay in large deep underground neutrino detector (DUNE)-like neutrino detectors. We introduced, for the first time in this kind of analysis, the experimentally confirmed neutrino oscillations of the atmospheric neutrino observations which reduce the corresponding background for the nucleon decay channel p -> mu(+) + pi(0) by a factor of 40%. Furthermore, we infer the impact of four systematics on such background: the overall efficiency, the muon reconstruction energy resolution, the resonant neutral pion cross-section, and the neutral pion angular resolution. Considering a 40 kton detector with efficiency of 45%, our analysis leads to an error band in the lower limit for the proton lifetime sensitivity, tau/B, from 7.9 x 10(33) years to 1.1 x 10(34) years at 90% confidence level (C.L.). These numbers can be compared with the current mode-dependent experimental limits tau > 10(31) - 10(33) years at 90% C.L.

JOURNAL OF PHYSICS G-NUCLEAR AND PARTICLE PHYSICS 46[7], 075006, 2019. DOI: 10.1088/1361-6471/ab0b56

[P259-2019] "Influence of silver electrochemically deposited onto zinc oxide seed nanoparticles on the photoelectrochemical performance of zinc oxide nanorod films"

Aranda, A.; **Landers, R.***; Carnelli, P.; Candal, R.; Alarcon, H.; Rodriguez, J.

The present article examines the synthesis and characterization of zinc oxide nanorods grown on zinc oxide and silver nanoparticle seeds. Zinc oxide seeds were electrodeposited on a support of fluorine-doped tin oxide glass and heat-treated at 380 degrees C. Silver nanoparticles were then deposited on this substrate, which was heat-treated at 160 degrees C. Their presence was confirmed using ultraviolet-visible spectroscopy, by observing an absorption peak around 400 nm, corresponding to surface plasmon resonance. Growth of zinc oxide nanorods was achieved in a chemical bath at 90 degrees C. The obtained films were analyzed by cyclic voltammetry, X-ray diffraction, and scanning electron microscopy. They consisted of zinc oxide with a Wurtzite-type crystal structure, arranged as nanorods of 50 nm. X-ray photoelectron spectroscopy exhibits peaks attributed to silver (0) and to the formation of silver oxide on the silver nanoparticle surface. In addition, two types of oxygen (O 1 s) were observed: oxygen from the crystalline network (O-2) and chemisorbed oxygen (-OH), for the seed and the nanorod films, respectively. The nanorods grown on zinc oxide seeds with silver deposits had a round shape and greater photoactivity than those grown without silver. This difference is attributed to the additional reflection that silver provides to the light reaching the film, thereby increasing the photogeneration from the charge carriers.

NANOMATERIALS AND NANOTECHNOLOGY 9, 1847980419844363, 2019. DOI: 10.1177/1847980419844363

[P260-2019] "Infrared electric field sampled frequency comb spectroscopy"

Kowligy, A. S.; Timmers, H.; Lind, A. J.; Elu, U.; **Cruz, F. C.***; Schunemann, P. G.; Biegert, J.; Diddams, S. A.

Probing matter with light in the mid-infrared provides unique insight into molecular composition, structure, and function with high sensitivity. However, laser spectroscopy in this spectral region lacks the broadband or tunable light sources and efficient detectors available in the visible or near-infrared. We overcome these challenges with an approach that unites a compact source of phase-stable, single-cycle, mid-infrared pulses with room temperature electric field-resolved detection at video rates. The ultrashort pulses correspond to laser frequency combs that span 3 to 27 mm (370 to 3333 cm(-1)), and are measured with dynamic range of >10(6) and spectral resolution as high as 0.003 cm(-1). We highlight the brightness and coherence of our apparatus with gas-, liquid-, and solid-phase spectroscopy that extends over spectral bandwidths comparable to thermal or infrared synchrotron sources. This unique combination enables powerful avenues for rapid detection of biological, chemical, and physical properties of matter with molecular specificity.

SCIENCE ADVANCES 5[6], eaaw8794, 2019. DOI: 10.1126/sciadv.aaw8794

[P261-2019] "Investigation of anisotropic fishing line-based phantom as tool in quality control of diffusion tensor imaging"

de Souza, E. M.*; Costa, E. T.; **Castellano, G.***

This work proposes a low-cost, fishing line-based phantom for quality control of diffusion tensor imaging (DTI). The device was applied to investigate the relationship between DTI indexes (DTIi) and imaging acquisition parameters. A Dyneema((R)) fishing line phantom was built with fiber bundles of different thicknesses. DTI acquisitions were performed in a 3T magnetic resonance imaging scanner using an 8-channel and a 32-channel head coil. For each coil, the following acquisition parameters were changed, one at a time: diffusion sensitivity factor (b value), echo time, sensitivity encoding, voxel size, number of signal averages, and number of diffusion gradient directions (NDGD). DTIi including fractional anisotropy, relative anisotropy (RA), linear anisotropy (CL), and planar anisotropy (CP) were calculated for each image; the data were analyzed using the coefficient of variation (CV) and distributions of DTIi values. The 32-channel head coil presented higher CV values for the DTIi RA, CL, and CP when voxel size was changed. Using the phantom, dependences between diffusion-related parameters (b value and NDGD) and DTIi were also observed; the majority of these were for the smaller thickness fiber bundles. The device proved to be useful for the verification of the DTI performance over time.

RADIOLOGICAL PHYSICS AND TECHNOLOGY 12[2], 161-171, 2019. DOI: 10.1007/s12194-019-00507-9

[P262-2019] "Is the H-0 tension suggesting a fourth neutrino generation?"

Carneiro, S.*; de Holanda, P. C.*; Pigozzo, C.; **Sobreira, F.***

Flavor oscillations experiments are suggesting the existence of a sterile, fourth neutrino generation with a mass of an eV order. This would mean an additional relativistic degree of freedom in the cosmic inventory, in contradiction with recent results from the Planck satellite, that have confirmed the standard value N-eff approximate to 3 for the effective number of relativistic species. On the other hand, the Planck best-fit for the Hubble-Lemaitre parameter is in tension with the local value determined with the Hubble Space Telescope, and adjusting N-eff is a possible way to overcome such a tension. In this paper we perform a joint analysis of three complementary cosmological distance rulers, namely the cosmic microwave backgroune acoustic scale measured by Planck, the baryonic acoustic oscillation scale model-independently determined by Verde et al., and luminosity distances measured with Joint Light-curves Analysis and Pantheon SNe Ia surveys. Two Gaussian priors were imposed to the analysis, the local expansion rate measured by Riess et al. and the baryon density parameter fixed from primordial nucleosynthesis by Cooke et al.. For the sake of generality and robustness, two different models are used in the tests, the standard Lambda CDM model and a generalized Chaplygin gas. The best-fit gives N-eff approximate to 4 in both models, with a Chaplygin gas parameter slightly negative, alpha approximate to -0.04. The standard value N--eff approximate to 3 is ruled out with approximate to 3 sigma.

PHYSICAL REVIEW D 100[2], 023505, 2019. DOI: 10.1103/PhysRevD.100.023505

[P263-2019] "Lambda(+)(C) production in pb-pb collisions at root S-NN=5.02 TeV"

Acharya, S.; Acosta, F. T.; Adamova, D.; **Albuquerque, D. S. D.*; Chinellato, D. D.*; De Souza, R. D.*; Takahashi, J.***; et. al.; ALICE Collaboration

A measurement of the production of prompt Lambda(+)(C) baryons in Pb-Pb collisions at root S-NN = 5.02 TeV with the ALICE detector at the LHC is reported. The Lambda(+)(C) and (Lambda) over bar (-)(C) were reconstructed at midrapidity (vertical bar y vertical bar < 0.5) via the hadronic decay channel Lambda(+)(C) -> pK(S)(0) (and charge conjugate) in the transverse momentum and centrality intervals 6 < p(T) < 12 GeV/c and 0-80%. The Lambda(+)(C)/D-0 ratio, which is sensitive to the charm quark hadronisation mechanisms in the medium, is measured and found to be larger than the ratio measured in minimum-bias pp collisions at root s = 7 TeV and in p-Pb collisions at root S-NN = 5.02 TeV. In particular, the values in p-Pb and Pb-Pb collisions differ by about two standard deviations of the combined statistical and systematic uncertainties in the common P-T interval covered by the measurements in the two collision systems. The Lambda(+)(C)/D-0 ratio is also compared with model calculations including different implementations of charm quark hadronisation. The measured ratio is reproduced by models implementing a pure coalescence scenario, while adding a fragmentation contribution leads to an underestimation. The Lambda(+)(C) nuclear modification factor, R-AA, is also presented. The measured values of the R-AA of Lambda(+)(C), D-S(+) and non-strange D mesons are compatible within the combined statistical and systematic uncertainties. They show, however, a hint of a hierarchy (R-AA(D0) < R-AA(DS+) < R--AA(Lambda C+)), conceivable with a contribution from coalescence mechanisms to charm hadron formation in the medium.

PHYSICS LETTERS B 793, 212-223, 2019. DOI: 10.1016/j.physletb.2019.04.046

[P264-2019] "Long term experience in Autonomous Stations and production quality control"

Lopes, L.; Alves, A. B.; Assis, P.; Blanco, A.; Carolino, N.; Cerda, M. A.; Conceicao, R.; Cunha, O.; **Dobrigkeit, C.***; Ferreira, M.; Fonte, P.; de Almeida, L.; Luz, R.; Martins, V. B.; Mendes, L.; Nogueira, J. C.; Pereira, A.; Pimenta, M.; Sarmento, R.; de Souza, V; Tome, B.

Large area arrays composed by dispersed stations are of major importance in experiments where Extensive Air Shower (EAS) sampling is necessary. In those dispersed stations, detectors that require very low maintenance and show good resilience to environmental conditions are mandatory.

In 2012, our group started to work in Resistive Plate Chambers that could become acceptable candidates to operate within these conditions. Since that time, more than 30 complete detectors were produced, tested and installed in different places, both indoor and outdoor. The data and analysis presented here are mainly related to the tests made in the Auger site in real conditions, where two Resistive Plate Chambers have been under test for more than two years. The results confirm the capability to operate such kind of Resistive Plate Chambers for long time periods under harsh conditions at a stable efficiency. In the last years, Laboratorio de Instrumentacao e Fisica Experimental de Particulas and USP-Sao Carlos have led a collaboration with the aim of installing an Engineering Array at BATATA (Auger) site to learn in more detail and improve the resilience and performance of the Resistive Plate Chambers in outdoor conditions. The organization of such collaboration and the work done so far will be presented.

JOURNAL OF INSTRUMENTATION 14, C07002, 2019. DOI: 10.1088/1748-0221/14/07/C07002

[P265-2019] "Longitudinal profiles of Extensive Air Showers with inclusion of charm and bottom particles"

Mueller, M. A.*; Goncalves, V. P.*

Charm and bottom particles are rare in Extensive Air Showers, but their effects can be radical on the EASs development. If such particles show up with a large fraction of primary energy, they can reach large atmospheric depths, depositing energy in deeper layers of the atmosphere. That will cause changes at the EAS observables (X-max, RMS and N-max), besides a considerable change in the shape of longitudinal profile energy deposit in the atmosphere. We are using for this work a modified code of an EAS simulator, CORSIKA, with production of charm and bottom particles at the first interaction of the primary cosmic ray. We will show in this paper some results to different x(F) values and different production models.

INTERNATIONAL JOURNAL OF MODERN PHYSICS A 34[12], 1950069, 2019. DOI: 10.1142/S0217751X19500696

[P266-2019] "Measurement of associated production of a W boson and a charm quark in proton-proton collisions at root s=13 Tev"

Sirunyan, A. M.; Tumasyan, A.; Adam, W.; **Chinellato, J. A.*; Tonelli Manganote, E. J.***; et. al.; CMS Collaboration

Measurements are presented of associated production of a W boson and a charm quark (W + c) in proton-proton collisions at a center-of-mass energy of 13 TeV. The data correspond to an integrated luminosity of 35.7 fb(-1) collected by the CMS experiment at the CERN LHC. The W bosons are identified by their decay into a muon and a neutrino. The charm quarks are tagged via the full reconstruction of D* (2010)(+/-) mesons that decay via D*(2010)(+/-) D-0 + pi(+/-) -> K--/+ + pi(+/-) + pi(+/-). A cross section is measured in the fiducial region defined by the muon transverse momentum p(T)(mu) > 26 GeV, muon pseudorapidity vertical bar eta(mu)vertical bar < 2.4, and charm quark transverse momentum p(T)(c) > 5 GeV. The inclusive cross section for this kinematic range is sigma(W + c) = 1026 +/- 31(stat)(-72)(+76) pb. The cross section is also measured differentially as a function of the pseudorapidity of the muon from the W boson decay. These measurements are compared with theoretical predictions and are used to probe the strange quark content of the proton.

EUROPEAN PHYSICAL JOURNAL C 79[3], 269, 2019. DOI: 10.1140/epjc/s10052-019-6752-1

[P267-2019] "Measurement of the splashback feature around SZ-selected Galaxy clusters with DES, SPT, and ACT"

Shin, T.; Adhikari, S.; Baxter, E. J.; **Sobreira, F.*;** et. al.

We present a detection of the splashback feature around galaxy clusters selected using the Sunyaev-Zel'dovich (SZ) signal. Recent measurements of the splashback feature around optically selected galaxy clusters have found that the splashback radius, rsp, is smaller than predicted by N-body simulations. Apossible explanation for this discrepancy is that rsp inferred from the observed radial distribution of galaxies is affected by selection effects related to the optical cluster-finding algorithms. We test this possibility by measuring the splashback feature in clusters selected via the SZ effect in data from the South Pole Telescope SZ survey and the Atacama Cosmology Telescope Polarimeter survey. The measurement is accomplished by correlating these cluster samples with galaxies detected in the Dark Energy Survey Year 3 data. The SZ observable used to select clusters in this analysis is expected to have a tighter correlation with halo mass and to be more immune to projection effects and aperture-induced biases, potentially ameliorating causes of systematic error for optically selected clusters. We find that the measured r(sp) for SZ-selected clusters is consistent with the expectations from simulations, although the small number of SZ-selected clusters makes a precise comparison difficult. In agreement with previous work, when using optically selected redMaPPer clusters with similar mass and redshift distributions, r(sp) is similar to 2 sigma smaller than in the simulations. These results motivate detailed investigations of selection biases in optically selected cluster catalogues and exploration of the splashback feature around larger samples of SZ-selected clusters. Additionally, we investigate trends in the galaxy profile and splashback feature as a function of galaxy colour, finding that blue galaxies have profiles close to a power law with no discernible splashback feature, which is consistent with them being on their first infall into the cluster.

MONTHLY NOTICES OF THE ROYAL ASTRONOMICAL SOCIETY 487[2], 2900-2918, 2019. DOI: 10.1093/mnras/stz1434

[P268-2019] "Measurements of the Higgs boson width and anomalous HVV couplings from on-shell and off-shell production in the four-lepton final state"

Sirunyan, A. M.; Tumasyan, A.; Adam, W.; **Chinellato, J. A.*; Tonelli Manganote, E. J.***; et. al.; CMS Collaboration

Studies of on-shell and off-shell Higgs boson production in the four-lepton final state are presented, using data from the CMS experiment at the LHC that correspond to an integrated luminosity of 80.2 fb(-1) at a center-of-mass energy of 13 TeV. Joint constraints are set on the Higgs boson total width and parameters that express its anomalous couplings to two electroweak vector bosons. These results are combined with those obtained from the data collected at center-of-mass energies of 7 and 8 TeV, corresponding to integrated luminosities of 5.1 and 19.7 fb(-1), respectively. Kinematic information from the decay particles and the associated jets are combined using matrix element techniques to identify the production mechanism and to increase sensitivity to the Higgs boson couplings in both production and decay. The constraints on anomalous HVV couplings are found to be consistent with the standard model expectation in both the on-shell and off-shell regions. Under the assumption of a coupling structure similar to that in the standard model, the Higgs boson width is constrained to be 3.2(-2.2)(+2.8)MeV while the expected constraint based on simulation is 4.1(-4.0)(+5.0) MeV. The constraints on the width remain similar with the inclusion of the tested anomalous HVV interactions.

PHYSICAL REVIEW D 99[11], 112003, 2019. DOI: 10.1103/PhysRevD.99.112003

[P269-2019] "Mode Structure in Superconducting Metamaterial Transmission-Line Resonators"

Wang, H.; Zhuravel, A. P.; Indrajeet, S.; Taketani, B. G.; Hutchings, M. D.; Hao, Y.; **Rouxinol, F.***; Wilhelm, F. K.; LaHaye, M. D.; Ustinov, A., V; Plourde, B. L. T.

Superconducting metamaterials are a promising resource for quantum-information science. In the context of circuit QED, they provide a means to engineer on-chip dispersion relations and a band structure that could ultimately be utilized for generating complex entangled states of quantum circuitry, for quantum-reservoir engineering, and as an element for quantum-simulation architectures. Here we report on the development and measurement at millikelvin temperatures of a particular type of circuit metamaterial resonator composed of planar superconducting lumped-element reactances in the form of a discrete left-handed transmission line that is compatible with circuit QED architectures. We discuss the details of the design, fabrication, and circuit properties of this system. As well, we provide an extensive characterization of the dense mode spectrum in these metamaterial resonators, which we conduct using both microwave-transmission measurements and laser-scanning microscopy. Results are observed to be in good quantitative agreement with numerical simulations and also an analytical model based upon current-voltage relationships for a discrete transmission line. In particular, we demonstrate that the metamaterial mode frequencies, spatial profiles of current and charge densities, and damping due to external loading can be readily modeled and understood, making this system a promising tool for future use in quantum-circuit applications and for studies of complex quantum systems.

PHYSICAL REVIEW APPLIED 11[5], 054062, 2019. DOI: 10.1103/PhysRevApplied.11.054062

[P270-2019] "Multiplicity dependence of (anti-)deuteron production in pp collisions at root s=7 TeV"

Acharya, S.; Acosta, F. T.; Adamova, D.; **Albuquerque, D. S. D.*; Chinellato, D. D.*; De Souza, R. D.*; Takahashi, J.***; et. al.; ALICE Collaboration

In this letter, the production of deuterons and anti-deuterons in pp collisions at root s = 7 TeV is studied as a function of the charged-particle multiplicity density at mid-rapidity with the ALICE detector at the LHC. Production yields are measured at mid-rapidity in five multiplicity classes and as a function of the deuteron transverse momentum (p(T)). The measurements are discussed in the context of hadron-coalescence models. The coalescence parameter B-2, extracted from the measured spectra of (anti-)deuteronsand primary (anti-)protons, exhibits no significant p(T)-dependence for p(T) < 3 GeV/c, in agreement with the expectations of a simple coalescence picture. At fixed transverse momentum per nucleon, the B-2 parameter is found to decrease smoothly from low multiplicity pp to Pb-Pb collisions, in qualitative agreement with more elaborate coalescence models. The measured mean transverse momentum of (anti-)deuterons in pp is not reproduced by the Blast-Wave model calculations that simultaneously describe pion, kaon and proton spectra, in contrast to central Pb-Pb collisions. The ratio between the p(T)-integrated yield of deuterons to protons, d/p, is found to increase with the charged-particle multiplicity, as observed in inelastic pp collisions at different centre-of-mass energies. The d/p ratios are reported in a wide range, from the lowest to the highest multiplicity values measured in pp collisions at the LHC.

PHYSICS LETTERS B 794, 50-63, 2019. DOI: 10.1016/j.physletb.2019.05.028

[P271-2019] "Nonequilibrium Free Energy Methods Applied to Magnetic Systems: The Degenerate Ising Model"

Cajahuaringa, S.*; Antonelli, A.*

In this paper, we review the physical concepts of the nonequilibrium techniques for the calculation of free energies applied to magnetic systems using Monte Carlo simulations of different nonequilibrium processes. The methodology allows the calculation of the free energy difference between two different system Hamiltonians, as well as the free energy dependence on temperature and magnetic field for a given Hamiltonian. As an illustration of the effectiveness of this approach, we apply the methodologies to determine the phase diagram of a simple microscopic model, the degenerate Ising model. Our results show very good agreement with those obtained from analytical (theoretical) methods.

JOURNAL OF STATISTICAL PHYSICS 175[5], 1006-1021, 2019. DOI: 10.1007/s10955-019-02267-7

[P272-2019] "On the relative bias of void tracers in the Dark Energy Survey"

Pollina, G.; Hamaus, N.; Paech, K.; **Sobreira, F.***; et. al.; DES Collaboration

Luminous tracers of large-scale structure are not entirely representative of the distribution of mass in our Universe. As they arise from the highest peaks in the matter density field, the spatial distribution of luminous objects is biased towards those peaks. On large scales, where density fluctuations are mild, this bias simply amounts to a constant offset in the clustering amplitude of the tracer, known as linear bias. In this work we focus on the relative bias between galaxies and galaxy clusters that are located inside and in the vicinity of cosmic voids, extended regions of relatively low density in the large-scale structure of the Universe. With the help of mock data we verify that the relation between galaxy and cluster overdensity around voids remains linear. Hence, the void-centric density profiles of different tracers can be linked by a single multiplicative constant. This amounts to the same value as the relative linear bias between tracers for the largest voids in the sample. For voids of small sizes, which typically arise in higher density regions, this constant has a higher value, possibly showing an environmental dependence similar to that observed for the linear bias itself. We confirm our findings by analysing data obtained during the first year of observations by the Dark Energy Survey. As a side product, we present the first catalogue of three-dimensional voids extracted from a photometric survey with a controlled photo-z uncertainty. Our results will be relevant in forthcoming analyses that attempt to use voids as cosmological probes.

MONTHLY NOTICES OF THE ROYAL ASTRONOMICAL SOCIETY 487[2], 2836-2852, 2019. DOI: 10.1093/mnras/stz1470

[P273-2019] "Performance of missing transverse momentum reconstruction in proton-proton collisions at root s=13 TeV using the CMS detector"

Sirunyan, A. M.; Tumasyan, A.; Adam, W.; **Chinellato, J. A.*; Tonelli Manganote, E. J.***; et. al.; CMS Collaboration

The performance of missing transverse momentum ((p) over right arrow (miss)(T)) reconstruction algorithms for the CMS experiment is presented, using proton-proton collisions at a center-of-mass energy of 13 TeV, collected at the CERN LHC in 2016. The data sample corresponds to an integrated luminosity of 35.9 fb(-1). The results include measurements of the scale and resolution of (p) over right arrow (miss)(T), and detailed studies of events identified with anomalous (p) over right arrow (miss)(T).

The performance is presented of a (p) over right arrow (miss)(T) reconstruction algorithm that mitigates the effects of multiple proton-proton interactions, using the "pileup per particle identification" method. The performance is shown of an algorithm used to estimate the compatibility of the reconstructed (p) over right arrow (miss)(T) with the hypothesis that it originates from resolution effects.

JOURNAL OF INSTRUMENTATION 14, P07004, 2019. DOI: 10.1088/1748-0221/14/07/P07004

[P274-2019] "Physical and micro-nano-structure properties of chromium nitride coating deposited by RF sputtering using dynamic glancing angle deposition"

Jimenez, M. J. M.*; Antunes, V.*; Cucatti, S.*; Riul, A., Jr.*; Zagonel, L. F.*; Figueroa, C. A.; **Wisnivesky, D.*; Alvarez, F.***

The CrN films were grown by rf-magnetron sputtering using a dynamic glancing angle deposition technique. In this technique, the substrate oscillates in front of the sputtering target with an angular amplitude and frequency commanded by a Programmable Logic Controller. The purpose of this paper is to study the physical properties of the CrN coatings deposited on crystalline silicon by using a square and linear dependence on time of the angle of oscillation of the substrate. The angular dependence of the atoms impinging on the substrate during the oscillation modified the flux and momentum transference to the films, forming a columnar wavy-like periodic structure depending on the customized oscillatory function. The influence of the oscillation on the physical properties of the materials such as morphology, residual stress, nano-hardness, crystallite size and texture of the columnar multi-components are reported. The angular dependence of the deposition technique opens the possibility to control, according to the specific application, the nanostructure, the of the hard coatings, the periodicity of the columnar films, the deposition rate of each period as well as the uniformity of the thickness of the CrN films. The technique can be applied to other hard coatings as well (e.g., TiN, TiCN and TiAlN). The flux F of atoms arriving on the substrate has a F similar to cos phi dependence on the impinging angle phi of the precursors. Considering that the compressive stress in hard coatings deposition depends, among other things, on both the substrate external bias and deposition rate, the technique offers a potentially useful possibility to tailor the compressive stress as well, which will be the subject of further research and applications.

SURFACE & COATINGS TECHNOLOGY 372, 268-277, 2019. DOI: 10.1016/j.surfcoat.2019.05.023

[P275-2019] "Physics with beam tau-neutrino appearance at DUNE"

de Gouvea, A.; Kelly, K. J.; **Stenico, G. V.*; Pasquini, P.***

We explore the capabilities of the upcoming Deep Underground Neutrino Experiment (DUNE) to measure nu(tau) charged-current interactions and the associated oscillation probability P(nu(mu) -> nu(tau)) at thorn at its far detector, concentrating on how such results can be used to probe neutrino properties and interactions. DUNE has the potential to identify significantly more nu(tau) events than all existing experiments and can use this data sample to nontrivially test the three-massive-neutrinos paradigm by providing complementary measurements to those from nu(e)-appearance nu(mu)-disappearance channels. We further discuss the sensitivity of the nu(tau)-appearance channel to several hypotheses for the physics that may lurk beyond the three-massive-neutrinos paradigm: a nonunitary lepton mixing matrix, the 3 + 1 light neutrinos hypothesis, and the existence of nonstandard neutral-current neutrino interactions. Throughout, we also consider the relative benefits of the proposed high-energy tune of the Long-Baseline Neutrino Facility (LBNF) beam line.

PHYSICAL REVIEW D 100[1], 016004, 2019. DOI: 10.1103/PhysRevD.100.016004

[P276-2019] "Pressure induced martensitic transition, magnetocaloric and magneto-transport properties in Mn-Ni-Sn Heusler alloy"

Sharma, J.; **Coelho, A. A.***; Repaka, D. V. M.; Ramanujan, R. V.; Suresh, K. G.

In this work, we report the effect of hydrostatic pressure (P) on the martensitic transition in Mn50Ni40Sn10 Heusler alloy using the magnetization and electrical resistivity measurements. Martensitic transition temperature (T-M) is found to shift significantly to higher temperatures with the application of pressure, which reflects the stabilization of the martensite phase. On the other hand, T-M shifts to lower temperatures with magnetic field, which implies the stabilization of the austenite phase. The estimated rate of change of martensitic transition temperature with pressure (dT(M)/dP) for the present alloy is similar to 4.6 K/kbar. The alloy shows a maximum negative magnetoresistance (MR) of 9.6% for P = 4 kbar at the martensitic transition. A large isothermal magnetic entropy change (Delta S-M) of 16.6 J/kg.K and a refrigerant capacity (RC) of similar to 146 J/kg are observed at TM under ambient pressure. Both quantities are found to decrease with the increase of pressure. The values of Delta S-M and adiabatic temperature change (Delta T-ad), calculated from heat capacity measurements are similar to 11.3 J/kg. K and -3.4 K respectively for 50 kOe field change. The observed pressure and field dependence results have been explained using the Clausius-Clapeyron equation. The combined effect of pressure and field on the martensitic transition is also discussed.

JOURNAL OF MAGNETISM AND MAGNETIC MATERIALS 487, UNSP 165307, 2019. DOI: 10.1016/j.jmmm.2019.165307

[P277-2019] "Production of the rho(770)(0) meson in pp and Pb-Pb collisions at root S-NN=2.76 TeV"

Acharya, S.; Acosta, F. T.; Adamova, D.; **Albuquerque, D. S. D.*; Chinellato, D. D.*; De Souza, R. D.*; Takahashi, J.***; et. al.; ALICE Collaboration

The production of the rho(770)(0) meson has been measured at midrapidity (vertical bar y vertical bar < 0.5) in pp and centrality differential Pb-Pb collisions at root S-NN = 2.76 TeV with the ALICE detector at the Large Hadron Collider. The particles have been reconstructed in the rho(770)(0) -> pi(+)pi(-) decay channel in the transverse-momentum (p(T)) range 0.5-11 GeV/c. A centrality-dependent suppression of the ratio of the integrated yields 2 rho(770)(0)/(pi(+)+pi(-)) is observed. The ratio decreases by similar to 40% from pp to central Pb-Pb collisions. A study of the p(T)-differential 2 rho(770)(0)/(pi(+) + pi(-)) ratio reveals that the suppression occurs at low transverse momenta, P-T < 2 GeV/c. At higher momentum, particle ratios measured in heavy-ion and pp collisions are consistent. The observed suppression is very similar to that previously measured for the K*(892)(0)/K ratio and is consistent with EPOS3 predictions that may imply that rescattering in the hadronic phase is a dominant mechanism for the observed suppression.

PHYSICAL REVIEW C 99[6], UNSP 064901, 2019. DOI: 10.1103/PhysRevC.99.064901

[P278-2019] "Putative hybridization gap in CaMn2Bi2 under applied pressure"

Piva, M. M.*; Thomas, S. M.; Fisk, Z.; Zhu, J-X; Thompson, J. D.; **Pagliuso, P. G.***; Rosa, P. F. S.

We report electrical transport measurements on CaMn2Bi2 single crystals under applied pressure. At ambient pressure and high temperatures, CaMn2Bi2 behaves as a single-band semimetal hosting Neel order at T-N = 150 K. At low temperatures, multiband behavior emerges along with an activated behavior typical of degenerate semiconductors. The activation gap is estimated to be Delta similar to 20 K. Applied pressure not only favors the antiferromagnetic order at a rate of 0.40(2) K/kbar, but it also enhances the activation gap at 20 kbar by about 70%. This gap enhancement is typical of correlated narrow-gap semiconductors such as FeSi and Ce3Bi4Pt3, and it places CaMn2Bi2 as a Mn-based hybridization-gap semiconductor candidate. Ab initio calculations based on density functional theory are shown to be insufficient to describe the ground state of CaMn2Bi2.

PHYSICAL REVIEW B 100[4], 045108, 2019. DOI: 10.1103/PhysRevB.100.045108

[P279-2019] "Radiation damage impact on hybrid-pixel detectors data"

Magalhaes, D. P.; **Rinkel, J.*; Tomal, A.***

This work aimed to quantify the influence of the deposited dose at the hybrid detector ASIC on the resulting image quality. Low (932 +/- 4 Gy) and high (6310 +/- 24 Gy) dose experiments were performed by irradiating a Medipix3RX single chip detector with the polychromatic beam from the Brazilian Synchrotron X-ray Imaging beamline. It was possible to evaluate subtle effects by using a noise component model based on estimating the quantum, electronic and structural noise contributions. Visible effects were quantified by analyzing the evolution of the histogram of the pixel counts at the irradiated area. The dose threshold for subtle damages was 388 +/- 3 Gy deposited in the gate oxide and shallow trench isolation oxide layers, while visible damages were observed for doses higher than 2635 +/- 15 Gy. A recovery of the damaged pixels with time was noticed and quantified, reaching the half-life time at 1.84 +/- 0.02 h after irradiation. These results encourage periodical maintenance procedures, for example through a new equalization matrix generation, which proved to be a possible tool for recovering the detector performance.

RADIATION PHYSICS AND CHEMISTRY 160, 63-67, 2019. DOI: 10.1016/j.radphyschem.2019.03.011

[P280-2019] "Real-time data processing in the ALICE High Level Trigger at the LHC"

Acharya, S.; Acosta, F. T.; Adamova, D.; **Albuquerque, D. S. D.*; Chinellato, D. D.*; De Souza, R. D.*; Takahashi, J.***; et. al.; ALICE Collaboration

At the Large Hadron Collider at CERN in Geneva, Switzerland, atomic nuclei are collided at ultra-relativistic energies. Many final-state particles are produced in each collision and their properties are measured by the ALICE detector. The detector signals induced by the produced particles are digitized leading to data rates that are in excess of 48 GB/s. The ALICE High Level Trigger (HLT) system pioneered the use of FPGA- and GPU-based algorithms to reconstruct charged-particle trajectories and reduce the data size in real time. The results of the reconstruction of the collision events, available online, are used for high level data quality and detector-performance monitoring and real-time time-dependent detector calibration. The online data compression techniques developed and used in the ALICE HLT have more than quadrupled the amount of data that can be stored for offline event processing.

COMPUTER PHYSICS COMMUNICATIONS 242, 25-48, 2019. DOI: 10.1016/j.cpc.2019.04.011

[P281-2019] "Relativistic Fluid Dynamics and its Extensions as an Effective Field Theory"

Montenegro, D.*; Ryblewski, R.; **Torrieri, G.***

We examine hydrodynamics from the perspective of an effective field theory. The microscopic scale in this case is the thermalization scale, and the macroscopic scale is the gradient, with thermal fluctuations playing the role of (sic). We argue that this method can be applied both, to consistently include thermal fluctuations in the theory and to extend hydrodynamics to systems whose microscopic structure is non-trivial. For the latter, we discuss the case of spin polarization and gauge theories.

ACTA PHYSICA POLONICA B 50[6], 1275-1288, 2019. DOI: 10.5506/APhysPolB.50.1275

[P282-2019] "Search for a heavy pseudoscalar boson decaying to a Z and a Higgs boson at root s=13TeV"

Sirunyan, A. M.; Tumasyan, A.; Adam, W.; **Chinellato, J. A.*; Tonelli Manganote, E. J.***; et. al.; CMS Collaboration

A search is presented for a heavy pseudoscalar boson A decaying to a Z boson and a Higgs boson with mass of 125 GeV. In the final state considered, the Higgs boson decays to a bottom quark and antiquark, and the Z boson decays either into a pair of electrons, muons, or neutrinos. The analysis is performed using a data sample corresponding to an integrated luminosity of 35.9 fb-1 collected in 2016 by the CMS experiment at the LHC from proton-proton collisions at a center-of-mass energy of 13 Te. The data are found to be consistent with the background expectations. Exclusion limits are set in the context of two-Higgs-doublet models in the A boson mass range between 225 and 1000.

EUROPEAN PHYSICAL JOURNAL C 79[7], 564, 2019. DOI: 10.1140/epjc/s10052-019-7058-z

[P283-2019] "Search for a low-mass tau(-)tau(+) resonance in association with a bottom quark in proton-proton collisions at root s=13 TeV"

Sirunyan, A. M.; Tumasyan, A.; Adam, W.; **Chinellato, J. A.*; Tonelli Manganote, E. J.***; et. al.; CMS Collaboration

A general search is presented for a low-mass (-+) resonance produced in association with a bottom quark. The search is based on proton-proton collision data at a center-of-mass energy of 13 TeV collected by the CMS experiment at the LHC, corresponding to an integrated luminosity of 35.9 fb(-1). The data are consistent with the standard model expectation. Upper limits at 95% confidence level on the cross section times branching fraction are determined for two signal models: a light pseudoscalar Higgs boson decaying to a pair of leptons produced in association with bottom quarks, and a low-mass boson X decaying to a -lepton pair that is produced in the decay of a bottom-like quark B such that B bX. Masses between 25 and 70 GeV are probed for the light pseudoscalar boson with upper limits ranging from 250 to 44 pb. Upper limits from 20 to 0.3 pb are set on B masses between 170 and 450 GeV for X boson masses between 20 and 70 GeV.

JOURNAL OF HIGH ENERGY PHYSICS 5, 210, 2019. DOI: 10.1007/JHEP05(2019)210

[P284-2019] "Search for a standard model-like Higgs boson in the mass range between 70 and 110 GeV in the diphoton final state in proton-proton collisions at root s=8 and 13 TeV"

Sirunyan, A. M.; Tumasyan, A.; Adam, W.; **Chinellato, J. A.*; Tonelli Manganote, E. J.***; et. al.; CMS Collaboration

The results of a search for a standard model-like Higgs boson in the mass range between 70 and 110 GeV decaying into two photons are presented. The analysis uses the data set collected with the CMS experiment in proton-proton collisions during the 2012 and 2016 LHC running periods. The data sample corresponds to an integrated luminosity of 19.7 (35.9) fb(-1) at root s = 8 (13) TeV. The expected and observed 95% confidence level upper limits on the product of the cross section and branching fraction into two photons are presented. The observed upper limit for the 2012 (2016) data set ranges from 129 (161) fb to 31 (26) fb. The statistical combination of the results from the analyses of the two data sets in the common mass range between 80 and 110 GeV yields an upper limit on the product of the cross section and branching fraction, normalized to that for a standard model-like Higgs boson, ranging from 0.7 to 0.2, with two notable exceptions: one in the region around the Z boson peak, where the limit rises to 1.1, which may be due to the presence of Drell-Yan dielectron production where electrons could be misidentified as isolated photons, and a second due to an observed excess with respect to the standard model prediction, which is maximal for a mass hypothesis of 95.3 GeV with a local (global) significance of 2.8 (1.3) standard deviations.

PHYSICS LETTERS B 793, 320-347, 2019. DOI: 10.1016/j.physletb.2019.03.064

[P285-2019] "Search for associated production of a Higgs boson and a single top quark in proton-proton collisions at root s=13 TeV"

Sirunyan, A. M.; Tumasyan, A.; Adam, W.; **Chinellato, J. A.*; Tonelli Manganote, E. J.***; et. al.; CMS Collaboration

A search is presented for the production of a Higgs boson in association with a single top quark, based on data collected in 2016 by the CMS experiment at the LHC at a center-of-mass energy of 13 TeV, which corresponds to an integrated luminosity of 35.9 fb(-1). The production cross section for this process is highly sensitive to the absolute values of the top quark Yukawa coupling, y(t); the Higgs boson coupling to vector bosons, g(HVV); and, uniquely, their relative sign. Analyses using multilepton signatures, targeting H -> WW, H -> tau tau, and H -> ZZ decay modes, and signatures with a single lepton and a b (b) over bar pair, targeting the H -> b (b) over bar decay, are combined with a reinterpretation of a measurement in the H -> gamma gamma channel to constrain y(t). For a standard model-like value of g(HVV), the data favor positive values of y(t) and exclude values of y(t) below about -0.9y(t)(SM).

PHYSICAL REVIEW D 99[9], 092005, 2019. DOI: 10.1103/PhysRevD.99.092005

[P286-2019] "Search for invisible decays of a Higgs boson produced through vector boson fusion in proton-proton collisions at root s=13 TeV"

Sirunyan, A. M.; Tumasyan, A.; Adam, W.; **Chinellato, J. A.*; Tonelli Manganote, E. J.***; et. al.; CMS Collaboration

A search for invisible decays of a Higgs boson is performed using proton-proton collision data collected with the CMS detector at the LHC in 2016 at a center-of-mass energy root s = 13 TeV, corresponding to an integrated luminosity of 35.9fb(-1). The search targets the production of a Higgs boson via vector boson fusion. The data are found to be in agreement with the background contributions from standard model processes. An observed (expected) upper limit of 0.33(0.25), at 95% confidence level, is placed on the branching fraction of the Higgs boson decay to invisible particles, assuming standard model production rates and a Higgs boson mass of 125.09GeV. Results from a combination of this analysis and other direct searches for invisible decays of the Higgs boson, performed using data collected at root s = 7, 8, and 13 TeV, are presented. An observed (expected) upper limit of 0.19(0.15), at 95% confidence level, is set on the branching fraction of invisible decays of the Higgs boson. The combined limit represents the most stringent bound on the invisible branching fraction of the Higgs boson reported to date. This result is also interpreted in the context of Higgs-portal dark matter models, in which upper bounds are placed on the spin-independent dark-matter-nucleon scattering cross section.

PHYSICS LETTERS B 793, 520-551, 2019. DOI: 10.1016/j.physletb.2019.04.025

[P287-2019] "Search for supersymmetry in events with a photon, jets, b-jets, and missing transverse momentum in proton-proton collisions at 13TeV"

Sirunyan, A. M.; Tumasyan, A.; Adam, W.; **Chinellato, J. A.*; Tonelli Manganote, E. J.***; et. al.; CMS Collaboration

A search for supersymmetry is presented based on events with at least one photon, jets, and large missing transverse momentum produced in proton-proton collisions at a center-of--mass energy of 13 TeV. The data correspond to an integrated luminosity of 35.9 fb -1 and were recorded at the LHC with the CMS detector in 2016. The analysis characterizes signal--like events by categorizing the data into various signal regions based on the number of jets, the number of b-tagged jets, and the missing transverse momentum. No significant excess of events is observed with respect to the expectations from standard model processes. Limits are placed on the gluino and top squark pair production cross sections using several simplified models of supersymmetric particle production with gauge-mediated supersymmetry breaking. Depending on the model and the mass of the nextto-lightest supersymmetric particle, the production of gluinos with masses as large as 2120 GeV and the production of top squarks with masses as large as 1230 GeV are excluded at 95% confidence level.

EUROPEAN PHYSICAL JOURNAL C 79[5], 2019. DOI: 10.1140/epjc/s10052-019-6926-x

[P288-2019] "Search for supersymmetry in final states with photons and missing transverse momentum in proton-proton collisions at 13 TeV"

Sirunyan, A. M.; Tumasyan, A.; Adam, W.; **Chinellato, J. A.*; Tonelli Manganote, E. J.***; et. al.; CMS Collaboration

Results are reported of a search for supersymmetry in final states with photons and missing transverse momentum in proton-proton collisions at the LHC. The data sample corresponds to an integrated luminosity of 35.9 fb(-1) collected at a center-of-mass energy of 13 TeV using the CMS detector. The results are interpreted in the context of models of gauge-mediated supersymmetry breaking. Production cross section limits are set on gluino and squark pair production in this framework. Gluino masses below 1.86 TeV and squark masses below 1.59 TeV are excluded at 95% confidence level.

JOURNAL OF HIGH ENERGY PHYSICS 6, 143, 2019. DOI: 10.1007/JHEP06(2019)143

[P289-2019] "Search for the associated production of the Higgs boson and a vector boson in proton-proton collisions at=13 TeV via Higgs boson decays to leptons"

Sirunyan, A. M.; Tumasyan, A.; Adam, W.; **Chinellato, J. A.*; Tonelli Manganote, E. J.***; et. al.; CMS Collaboration

A search for the standard model Higgs boson produced in association with a W or a Z boson and decaying to a pair of leptons is performed. A data sample of proton-proton collisions collected at p s = 13TeV by the CMS experiment at the CERN LHC is used, corresponding to an integrated luminosity of 35.9 fb. The signal strength is measured relative to the expectation for the standard model Higgs boson, yielding = 2: 5 +1:4. These results are combined with earlier CMS measurements targeting Higgs boson decays to a pair of leptons, performed with the same data set in the gluon fusion and vector boson fusion production modes. The combined signal strength is = 1: 24 +0:29 (1: 00 +0:24 expected), and the observed signi fi cance is 5.5 standard deviations (4.8 expected) for a Higgs boson mass of 125GeV.

JOURNAL OF HIGH ENERGY PHYSICS 6, 093, 2019. DOI: 10.1007/JHEP06(2019)093

[P290-2019] "Sedimentary provenance of the Marilia Formation (Bauru Basin), Southeast Brazil"

dos Santos, C. A. M.; Batezelli, A.; **Nakasuga, W. M.***; Resende, R. S.; Saenz, Carlos A. T.; Nunes, J. O. R.

The Marilia Formation is a lithostratigraphic unit positioned at the top of the Bauru Group of Maastrichtian age. The present work presents a provenance study of the Marilia Formation sandstones through the combined dating of the fission-track method (FTM) and U-Pb, in which individual zircon grains are simultaneously dated by these two methods. Thirty-one zircons were dated in the C5 sample and 26 in the C7 sample for a total of 57 grains. The data demonstrated a wide range of U-Pb ages, presenting maximum and minimum ages, respectively: 2,905 +/- 11 and 128 +/- 1 Ma for the C7 sample and 2,676 +/- 10 and 455 +/- 5 Ma for the C5 sample. Regarding the fission-track (FT) ages, they have been grouped into three time intervals, which are associated to geological events relatively well recognized in the published literature: ages younger than 250 Ma (Wealdenian Reactivation); between 250 and 470 Ma (Palaeozoic orogenesis-Ocloyic, Precordilleran, Chanic, and Sanrafaelic); and older than 470 (Precambrian collisions-Brasiliano I, II, and III). There is a predominance of results of Precambrian age using the U-Pb dating, mainly in the Neopalaeoproterozoic, and with FT dating corresponding to the Ocloyic, Precordilleran, Chanic, and Sanrafaelic orogeneses. From the comparison of the results between the two dating methods, the age variations suggest that the zircons originated during the main south-western orogenesis of Gondwana and were reworked during the Palaeozoic and Mesozoic geological episodes. The ages associated to the Upper Cretaceous are related to the tectonic and magmatic activity of the Alto Paranaiba Uplift.

GEOLOGICAL JOURNAL 1-17, 2019. DOI: 10.1002/gj.3576

[P291-2019] "Studies of Beauty Suppression via Nonprompt D-0 Mesons in Pb-Pb Collisions at root s(NN)=5.02 TeV"

Sirunyan, A. M.; Tumasyan, A.; Adam, W.; **Chinellato, J. A.*; Tonelli Manganote, E. J.***; et. al.; CMS Collaboration

The transverse momentum spectra of D-0 mesons from b hadron decays are measured at midrapidity (vertical bar y vertical bar < 1) in pp and Pb-Pb collisions at a nucleon-nucleon center of mass energy of 5.02 TeV with the CMS detector at the LHC. The D-0 mesons from b hadron decays are distinguished from prompt D-0 mesons by their decay topologies. In Pb-Pb collisions, the B -> D-0 yield is found to be suppressed in the measured p(T) range from 2 to 100 GeV/c as compared to pp collisions. The suppression is weaker than that of prompt D-0 mesons and charged hadrons for p(T) around 10 GeV/c. While theoretical calculations incorporating partonic energy loss in the quark-gluon plasma can successfully describe the measured B -> D-0 suppression at higher p(T), the data show an indication of larger suppression than the model predictions in the range of 2 < p(T) < 5 GeV/c.

PHYSICAL REVIEW LETTERS 123[2] 022001, 2019. DOI: 10.1103/PhysRevLett.123.022001

[P292-2019] "Study of Electron Transport in 4H-SiC by Using Nonequilibrium Statistical Ensemble Formalism"

Vasconcelos, J. L.; Rodrigues, C. G.; **Luzzi, R.***

A theoretical study, by using Nonequilibrium Statistical Ensemble Formalism (NESEF), on the nonlinear transport of electrons in the transient and steady state of n-doped 4H-SiC under the influence of high electric fields is presented. The electron drift velocity and the nonequilibrium temperature are obtained, and their dependence on the electric field applied in the orientation parallel or perpendicular to the c-axis is derived and analyzed.

BRAZILIAN JOURNAL OF PHYSICS 49[4], 494-501, 2019. DOI: 10.1007/s13538-019-00661-w

[P293-2019] "Superluminous supernovae from the Dark Energy Survey"

Angus, C. R.; Smith, M.; Sullivan, M.; **Sobreira, F.***; et. al.; DES Collaboration

We present a sample of 21 hydrogen-free superluminous supernovae (SLSNe-I) and one hydrogen-rich SLSN (SLSN-II) detected during the five-year Dark Energy Survey (DES). These SNe, located in the redshift range 0.220 < z < 1.998, represent the largest homogeneously selected sample of SLSN events at high redshift. We present the observed g, r, i, z light curves for these SNe, which we interpolate using Gaussian processes. The resulting light curves are analysed to determine the luminosity function of SLSNe-I, and their evolutionary time--scales. The DES SLSN-I sample significantly broadens the distribution of SLSN-I light-curve properties when combined with existing samples from the literature. We fit a magnetar model to our SLSNe, and find that this model alone is unable to replicate the behaviour of many of the bolometric light curves. We search theDES SLSN-I light curves for the presence of initial peaks prior to the main light-curve peak. Using a shock breakout model, our Monte Carlo search finds that 3 of our 14 eventswith pre-max data display such initial peaks. However, 10 events showno evidence for such peaks, in some cases downto an absolutemagnitude of <-16, suggesting that such features are not ubiquitous to all SLSN-I events. We also identify a red pre-peak feature within the light curve of one SLSN, which is comparable to that observed within SN2018bsz.

MONTHLY NOTICES OF THE ROYAL ASTRONOMICAL SOCIETY 487[2], 2215-2241, 2019. DOI: 10.1093/mnras/stz1321

[P294-2019] "Syngas production by dry reforming of methane using lyophilized nickel catalysts"

Moura-Nickel, C. D.; Tachinski, C. G.; **Landers, R.***; De Noni Jr., A.; Virmond, E.; Peterson, M.; Moreira, R. F. P. M.; Jose, H. J.

In this work, lyophilized nickel catalysts were synthesized and compared with a commercial catalyst (CCom) in the process of dry reforming of methane. Ni-Al2O3 catalysts were prepared by epoxide-initiated gelation method and lyophilized with different percentage of active phase: 5 wt% (LNi5), 10 wt% (LNi10), 15 wt% (LNi15) and 20 wt% (LNi20). The catalysts were characterized by physical nitrogen adsorption, infrared spectroscopy, X-ray diffractometry, scanning electron microscopy and X-ray photoelectron spectroscopy. The catalytic tests were performed at 600 degrees C, 700 degrees C and 800 degrees C. All catalysts were active in the reforming reactions except the LNi5 and CCom catalysts at temperatures of 600 degrees C and 700 degrees C. The LNi10 catalyst at 800 degrees C has presented the highest syngas production. The CCom showed the highest carbon deposition at 600 degrees C with 2.26 mg which represents 4.52% of the initial weight of the catalyst. Increasing the nickel content from 5 wt% to 10 wt% resulted in a syngas gain of 1.31 mu mol/min, 0.86 mu mol/min and 1.25 mu mol/min at 600 degrees C, 700 degrees C and 800 degrees C, respectively. The increase of the active phase from 10 wt% to 15 wt% and 20 wt% did not present significant effects in the syngas production. The lyophilization process in the drying stage of the catalyst has proved to be quite satisfactory in the dry reforming of methane.

CHEMICAL ENGINEERING SCIENCE 205, 74-82, 2019. DOI: 10.1016/j.ces.2019.04.035

[P295-2019] "Transcranial Optical Monitoring of Cerebral Hemodynamics in Acute Stroke Patients during Mechanical Thrombectomy"

Forti, R. M.*; Favilla, C. G.; Cochran, J. M.; Baker, W. B.; Detre, J. A.; Kasner, S. E.; Mullen, M. T.; Messe, S. R.; Kofke, W. A.; Balu, R.; Kung, D.; Pukenas, B. A.; Sedora-Roman, N. I.; Hurst, R. W.; Choudhri, O. A.; **Mesquita, R. C.***; Yodh, A. G.

Introduction: Mechanical thrombectomy is revolutionizing treatment of acute stroke due to large vessel occlusion (LVO). Unfortunately, use of the modified Thrombolysis in Cerebral Infarction score (mTICI) to characterize recanalization of the cerebral vasculature does not address microvascular perfusion of the distal parenchyma, nor provide more than a vascular "snapshot." Thus, little is known about tissue-level hemodynamic consequences of LVO recanalization. Diffuse correlation spectroscopy (DCS) and diffuse optical spectroscopy (DOS) are promising methods for continuous, noninvasive, contrast-free transcranial monitoring of cerebral microvasculature. Methods: Here, we use a combined DCS/DOS system to monitor frontal lobe hemodynamic changes during endovascular treatment of 2 patients with ischemic stroke due to internal carotid artery (ICA) occlusions. Results and Discussion: The monitoring instrument identified a recanalization-induced increase in ipsilateral cerebral blood flow (CBF) with little or no concurrent change in contralateral CBF and extracerebral blood flow. The results suggest that diffuse optical monitoring is sensitive to intracerebral hemodynamics in patients with ICA occlusion and can measure microvascular responses to mechanical thrombectomy.

JOURNAL OF STROKE & CEREBROVASCULAR DISEASES 28[6], 1483-1494, 2019. DOI: 10.1016/j.jstrokecerebrovasdis.2019.03.019B5$C

Eventos publicados

[P296-2019] "Complex network changes during a virtual reality rehabilitation protocol following stroke: a case study"

Feitosa, J. A.*; Stefano Filho, C. A.*; Casseb, R. F.; Camargo, A.; Martins, B. S. G.; Ballester, B. R.; Omedas, P.; Verschure, P.; Oberg, T. D.; Min, L. L.; **Castellano, G.***

Stroke is one of the main causes of disabilities caused by injuries to the human central nervous system, yielding a wide range of mild to severe impairments that can compromise sensorimotor and cognitive functions. Although rehabilitation protocols may improve function of stroke survivors, patients often reach plateaus while undergoing therapy. Recently, virtual reality (VR) technologies have been paired with traditional rehabilitation aiming to improve function recovery after stroke. Aiming to better understand structural brain changes due to VR rehabilitation protocols, we modeled the brain as a graph and extracted three measures representing the network's topology: degree, clustering coefficient and betweenness centrality (BC). In this single case study, our results indicate that all metrics increased on the ipsilesional hemisphere, while remaining about the same at the contralesional site. Particularly, the number of functional connections increased in the lesion area overtime. In addition, the BC displayed the highest variations, and in brain regions related to the patient's cognitive and motor impairments; hence, we argue that this measure could be regarded as an indicative for brain plasticity mechanisms.

9TH INTERNATIONAL IEEE/EMBS CONFERENCE ON NEURAL ENGINEERING (NER) International IEEE EMBS Conference on Neural Engineering 891-894, MAR 20-23, 2019.

[P297-2019] "Innovative instruments based on cryogenically cooled silicon crystals for the CARNAUBA beamline at Sirius-LNLS"

Tolentino, H. C. N.; Soares, M. M.; **Silva, F. M. C.***; Rezende, J. H.; Puglia, D.; Bordin, A.; Silva, M. S.; Geraldes, R. R.

The CARNAUBA beamline is the tender-to-hard X-ray nanoprobe under construction for the new source Sirius at the Brazilian Synchrotron Light Laboratory (LNLS). The all achromatic optics relies on KB mirrors and a horizontal secondary source aperture (SSA) to reach beam size down to 30x30 nm2 at the sample position. To handle the power on the optical elements the choice has been to build instruments based on cryogenically cooled Si crystals. These optical elements X-ray diagnostic, primary mirrors, secondary source aperture and monochromator and expected performance are described here.

13TH INTERNATIONAL CONFERENCE ON SYNCHROTRON RADIATION INSTRUMENTATION (SRI2018) AIP Conference Proceedings 2054, 060026, JUN 10-15, 2018, 2019. DOI:10.1063/1.5084657

***Autores da comunidade IFGW**
Fonte: Web of Science on-line (WOS)

Defesas de Teses do IFGW

[T007-2019] "Transferência, geração e monitoração de emaranhamento quântico em sistemas compostos por átomos acoplados a cavidades microtoroidais"
Aluno: Emílio Henrique dos Santos Sousa
Orientador: Prof. Dr. José Antonio Roversi
Data: 18/07/2019

Defesas de Dissertações do IFGW

[D015-2019] "Quantum fluctuations in non-globally hyperbolic spacetimes"
Aluno: Vitor Barroso Silveira
Orientador: Prof. Dr. João Paulo Pitelli Manoel
Data: 15/08/2019

Fonte: Portal IFGW/Pós-graduação - Agenda de Colóquios, Defesas e Seminários.
Disponível em: http://portal.ifi.unicamp.br/pos-graduacao

***Nestes meses não há Defesas de Dissertações e Teses do PECIM com Orientadores do IFGW.**

Fique atento!
Em breve nosso Boletim Abstracta IFGW mudará o seu endereço de acesso.

Abstracta

Instituto de Física
Diretor: Prof. Dr. Pascoal José Giglio Pagliuso
Diretora Associada: Profa. Dra. Mônica Alonso Cotta
Universidade Estadual de Campinas - UNICAMP
Cidade Universitária Zeferino Vaz
13083-859 - Campinas - SP - Brasil
e-mail: secdir@ifi.unicamp.br
Fone: +55 19 3521-5300

Publicação

Biblioteca do Instituto de Física Gleb Wataghin
http://portal.ifi.unicamp.br/biblioteca

Diretora Técnica: Sandra Maria Carlos Cartaxo
Coordenadora da Comissão de Biblioteca: Profa. Dra. Arlene Cristina Aguilar

Elaboração:
Maria Graciele Trevisan (Bibliotecária)
Ayres Neri da Cunha Junior (Técnico Administrativo)
contato: infobif@ifi.unicamp.br